# Thermal isomerization of phenylazoindoles

Hegedüsová, Lea; Kutel', Rastislav; Medved', Miroslav; Pašteka, Lukáš Félix; Cigáň, Marek; Budzák, Šimon

*Published in:*
International Journal of Quantum Chemistry

*DOI:*
10.1002/qua.27120



*Publication date:*
2023

Received: 29 November 2022 | Revised: 12 February 2023 | Accepted: 20 February 2023

DOI: 10.1002/qua.27120

RESEARCH ARTICLE

International Journal of Quantum Chemistry WILEY

# Thermal isomerization of phenylazoindoles: Inversion or rotation? That is the question

Lea Hegedüsová[1] | Rastislav Kutel'[1] | Miroslav Medved'[2,3] | Lukáš Félix Pašteka[4,5] | Marek Cigáň[1] | Šimon Budzák[3]

[1]Department of Organic Chemistry, Faculty of Natural Sciences, Comenius University, Ilkovičova 6, 84215 Bratislava, Slovakia

[2]Regional Centre of Advanced Technologies and Materials, Czech Advanced Technology and Research Institute, Palacký University Olomouc, Křížkovského 8, 77900 Olomouc, Czechia

[3]Department of Chemistry, Faculty of Natural Sciences, Matej Bel University, Tajovského 40, 97401 Banská Bystrica, Slovakia

[4]Van Swinderen Institute for Particle Physics and Gravity, University of Groningen, Nijenborgh 4, 9747 AG Groningen, The Netherlands

[5]Department of Physical and Theoretical Chemistry, Faculty of Natural Sciences, Comenius University, Ilkovičova 6, 84215 Bratislava, Slovakia

**Correspondence**
Marek Cigáň, Department of Organic Chemistry, Faculty of Natural Sciences, Comenius University, Ilkovičova 6, 84215 Bratislava, Slovakia.
Email: marek.cigan@uniba.sk

Šimon Budzák, Department of Chemistry, Faculty of Natural Sciences, Matej Bel University, Tajovského 40, 97401, Banská Bystrica, Slovakia.
Email: simon.budzak@umb.sk

**Funding information**
Agentúra na Podporu Výskumu a Vývoja, Grant/Award Number: APVV-20-0098; Vedecká Grantová Agentúra MŠVVaŠ SR a SAV, Grant/Award Number: VEGA 1/0562/20

## Abstract

Azoheteroarenes represent an attractive group of photochromes exhibiting a large structural variability and tunability of photoswitching characteristics. The thermal back-isomerization can proceed via inversion or rotation mechanisms, depending on the functionalization and environment. However, the distinction between the two remains a challenge for both experiment and theory. Here, four experimentally fully characterized phenylazoindoles are studied to establish the mechanism of back-reaction in solvent using density functional theory (DFT), spin-flip time-dependent (TD-)DFT, mixed-reference TD-DFT, and restricted ensemble Kohn–Sham approaches as well as CASPT2 and CCSD(T). While the inversion is consistently described by all methods, the rotation mechanism requires multireference approaches including dynamic correlation. The balanced description of both pathways becomes even more important in solvent which apparently affects the mechanism. For the present set, the range-separated functionals combined with continuum models appear to be the most consistent with experiment in terms of the substitutional and solvent effects on thermal halftimes.

**KEYWORDS**
azoindoles, correlation energy, density functional theory, multireference methods, thermal isomerization

## 1 | INTRODUCTION

Azobenzenes (AZBs) are one of the oldest known molecular photoswitches [1] meaning molecules able to reversibly transform between two forms, at least in one direction after photoexcitation. AZB can exist as *Z* and *E* isomers, the latter being more stable. The photoexcitation of the *E* isomer and subsequent relaxation in the excited state populates the less stable *Z* isomer. The back-isomerization can proceed via a photochemical pathway or thermally on the ground state (GS) potential energy surface.

Thermal half-lives of *Z*-azobenzenes are highly variable [2–4], which renders them suitable for diverse applications. They can be as short as 40 ns [5], which is important for medical applications such as vision restoration, where the rapid response to a visual signal together with the fast recovery of the original state of receptor are vital to achieve the required biological effect [6]. Other photo-pharmaceutical applications prefer

  

bistable azobenzenes with a high thermal barrier exhibiting light triggered switching in both directions. Lately, tetrafluoro- and tetrachloro-azobenzenes [7, 8] offered such a property. *In vivo* applications require that the photon could reach the photoswitch inside the organism. In this aspect, azonium-based switches are promising since they absorb the deep penetrating red and near-IR photons [9]. Details about the development of azobenzene photoswitches could be found in recent reviews by Beharry and Woolley [10], Jerca [1], Fedele [11], Cheng [12], Bandara [13], and others.

The thermal isomerization of AZB photoswitches can proceed via two different competing mechanisms. Inversion mechanism, characterized by the linear arrangement of the N═N—C bonds in the transition state ($TS_{inv}$), is endorsed by preserving the double N═N bond but involves an $sp^2$-to-$sp$ hybridization change on one of the nitrogens. Rotation or torsion mechanism, on the other hand, is characterized by a 90° C—N═N—C dihedral angle in the respective transition state ($TS_{rot}$), thus breaking the π component of the N═N bond, however not requiring the change of the hybridization. Computationally, the comparison between $TS_{inv}$ and $TS_{rot}$ is challenging. The former is well described by a single Slater determinant, and the correct description of the dynamic correlation is the main issue addressed by more advanced *ab initio* methods. The rotation transition state features near-degenerate highest occupied molecular orbital (HOMO) and lowest unoccupied molecular orbital (LUMO) necessitating a multireference (MR) approach. For chemically relevant medium-sized molecules, density functional theory (DFT) methods have usually been applied due to computational efficiency. However, in this framework, one can obtain different inversion/rotation ordering based on the choice of spin-restricted/unrestricted Kohn–Sham (KS) formalism. If one applies restricted KS (RKS), $TS_{rot}$ becomes disadvantaged compared to $TS_{inv}$. This could be resolved by allowing α and β electrons to have different spatial distribution, which is known as the unrestricted (U) KS approach. UKS usually brings stabilization of $TS_{rot}$ at the price of large spin contamination. For experiment, the knowledge of the reaction mechanism is highly relevant when it comes to interpretation, but the accurate prediction of the $\Delta G^{\ddagger}$ values is even more important since it allows computational tuning of the thermal reaction rate, according to the needs of a specific application.

Next, we highlight some of the large number of theoretical works on modeling of the thermal reaction barrier of the azobenzenes. For a more extended list of computational studies of azobenzenes, see, for example, reviews [13, 14].

Orlandi and coworkers in their influential work suggested the torsional movement as a preferential pathway for the thermal back-isomerization of AZB using complete active space second-order perturbation theory (CASPT2) in combination with the 6-31G(d) basis set [15].

Large exploration of azobenzene chemical space was performed by Dokić et al. [16] who calculated 90 different substituents at the B3LYP/6-31G(d) level. It was found that in most cases the reaction proceeds via inversion, while the rotation mechanism occurs for *push-pull* molecules in the polar environments. The choice of a global hybrid functional is quite usual in for azobenzene studies.

Recently, heteroaryl azo dye photoswitches have attracted research attention particularly due to their broader structural variability (including possible hydrogen bonding or metal coordination) that is often reflected in their photochromic behavior. Fuchter and coworkers [2, 17] improved the photochemical and thermal properties of AZB by substituting one of the phenyl groups with a heteroarene cycle. This idea [2] was followed by a large number of calculations relying on the PBE0-D3/6-31G(d,p) method, and the inversion was found as the most accessible back-isomerization pathway. *Ortho*-aminated arylazopyrazoles showed good thermal stability accompanied by favorable separation of absorption bands; the *E*-to-*Z* transformation could be achieved by blue light, while the photochemical back-reaction could be performed by red light, with the thermal stability of the *Z* isomer of 10 days [18]. No calculations were performed but authors referred to a previous combinatorial study from the Fuchter group [19], based on the above described protocol. These works illustrate the synergy between experiment and theory in this young and expanding field. The thermal barrier was also computed for azobispyrazoles at the PBE0-D3BJ/6-31G(d,p) level [20], employing the UKS and RKS approaches for the rotation and inversion TSs, respectively, and the rotation was identified as the main back-isomerization route. In the study of phenylazoindoles, the long-range corrected functional with empirical dispersion, ωB97X-D, was used with the TZVP basis set, and the UKS approach was applied to $TS_{rot}$. The isomerization to hydrazone was also studied in the protic environments [21]. The same group showed [22] that for a structurally simple phenylazoindole photoswitch thermal isomerization rate could be tuned from nanoseconds to days by a methyl group substitution and/or the change of solvent. Especially water molecules were found to promote the tautomerization of AZB to hydrazone by facilitating the N—N bond rotation. Rotation was also identified as the main back-reaction mechanism for difluoro-dichloro-azobenzenes using the M06-2X functional with an additional dispersion correction (D3) and the 6-31+G(d,p) basis set.

Benchmarking DFT functionals [23] against experimental $\Delta G^{\ddagger}$ values for a series of *Z*-azoarenes revealed that out of the tested functionals, PBE0-D3BJ and MN12-SX combined with the 6-311+G(d,p) basis set predicted most reliably the relative reactivity of azoarenes. The authors also noted that the usage of basis sets of triple-ζ quality with diffuse and polarization functions brings only a small improvement with large computational cost.

In the work of Poutanen et al. [24], hydroxyazobenzenes were used as vapor sensors. When explaining their different isomerization behavior important for the function of the sensor, the authors pointed to the change of the reaction mechanism invoked by altering the solvent polarity. Mužalo et al. further highlighted the role of the environment in biological applications [25], where AZBs usually occur in complex biological structures affecting the accessibility of some reaction pathways. Interestingly, a QM/MM scheme using DFT for description of AZB and molecular mechanics for the environment was able to capture the inversion/rotation change in mechanism of *push-pull* AZBs when going to more polar DMSO solvent.

The studies described above clearly demonstrate the dominant application of RKS/UKS methodologies in the calculation of activation energies for AZBs, with different mechanisms of thermal reaction suggested as most probable. In some cases, a particular conclusion could be an artifact of used RKS/UKS methodology while authors not always clearly stated how the $TS_{rot}$ structure/energy was obtained. In the last years, theoretical chemistry saw a remarkable development of new methods combining the power of multireference methods with DFT. In the multiconfiguration pair-DFT (MC-PDFT), the kinetic and Coulomb energy contributions as well as so called on-top-density-functional energy are evaluated using the total electron density, its gradient, and the on-top pair density derived from the CASSCF wavefunction [26, 27]. Spin-restricted ensemble-referenced Kohn–Sham (REKS) method uses several references to obtain well-defined density for strongly correlated systems in the ground and excited states [28]. Spin-flip time-dependent DFT (SF-TDDFT) [29, 30] starting from a single component of the triplet state as the reference can describe $TS_{rot}$ as the lowest singlet state avoiding any convergence issues typical for RKS at such a point, however, it often suffers from a large spin contamination. Recently, mixed-reference spin-flip time-dependent density functional theory (MRSF-TDDFT) has been proposed and implemented [31]. Unlike original SF-TDDFT, MRSF-TDDFT uses a mixed-reference reduced density matrix derived from two components ($M_S = \pm 1$) of the triplet state and is expected to be almost spin-contamination-free. The REKS and MRSF-TDDFT methods bring a promise of small spin-contamination and more balanced description of $TS_{inv}/TS_{rot}$ for azobenzenes. Nevertheless, they also still carry the question of a DFT functional choice. In this work, we compare results of these methods with the *ab initio* CASPT2 [32, 33] and DLPNO-CCSD(T) [34] methods. In addition, advances in the development of MR-CCSD(T) methods [35, 36] allowed us to compare our results against the gold standard of computational chemistry.

As our test set, we chose four phenylazoindole derivatives (Figure 1). Although 3-(phenyldiazenyl)-1*H*-indoles $M_0$ and $M_1$ are known compounds with determined photochromic characteristics, we believe that observed unexpected and significant decrease in rate of back thermal isomerization with increasing *push-pull* character of a skeleton deserves deeper investigation. To the best of our knowledge, the photoswitching properties of compounds $M_2$ and $M_3$ have never been studied before. The *N*-methyl derivative $M_2$ was chosen to evaluate a role of possible intermolecular hydrogen-bond mediated acceleration of back thermal reaction of $M_1$ in polar environment. On the other hand, the photoswitch $M_3$ bearing strong electron-donating *p*-amino group is a new compound that offers the possibility to assess the opposite electronic effect of the *p*-substituent on the overall photoswitching behavior.

The manuscript is organized as follows: first the used theoretical and experimental methodologies are described. Next, the results of gas phase benchmark calculations of the thermal *Z*-to-*E* reaction for $M_0$ are presented. Subsequently, all molecules are analyzed using previously selected methods, focusing on the solvent effects and trends in the set. The comparison and balanced description of the torsion and inversion mechanisms for the normal forms of $M_0$–$M_3$ are our main target since, as we discuss latter, comparable reaction characteristics of $M_1$ and $M_2$ make the tautomerization reaction involving zwitterions unlikely.

## 2 | METHODS

### 2.1 | Theoretical methods

Geometry optimizations of all stable structures were performed using the M06-2X functional [37] and the def2-TZVP basis set [38] within the RKS formalism. Numerical instabilities of this functional are well known, therefore we used an ultrafine integration grid (99590). Each localized minimum was checked by calculating the Hessian, always finding the positive definitive matrix. The studied molecules have several degrees of freedom, but the conformational space was small enough to be sampled manually (see Data S1 for xyz coordinates of all structures). In the $TS_{inv}$ search, we generated initial structures manually starting from previously obtained local minima and changing the C—N═N angle to 180°. Alternatively, C—N═N—C dihedral angle was set to 90° to obtain an initial guess of $TS_{rot}$. From each local minimum, we obtained two inversion TSs and

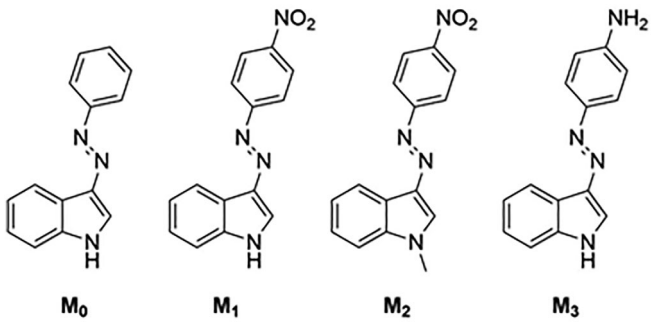


**FIGURE 1** Studied phenylazoindoles.

one rotation TS. The TS optimizations led to structures with a single imaginary frequency which indicated a true first order saddle point for the transformation of reactants to products. For the $TS_{rot}$, the UKS approach was used. All optimizations were performed considering the benzene (Bz) and DMSO solvents described by the integral equation formalism variant of the polarizable continuum model (IEF-PCM) [39].

The structures obtained in this way were then used in a series of single-point calculations in the gas phase:

1. UKS calculations were performed for all stationary points, with semiempirical INDO orbitals used as an initial guess. HOMO and LUMO were mixed to ensure breaking the $\alpha/\beta$ symmetry. For all structures but $TS_{rot}$, UKS converged to RKS solution.
2. RKS calculations were performed in $TS_{rot}$ geometries.
3. SF-TDDFT was used starting from a restricted open-shell (ROKS) triplet reference, requesting five SF-TDDFT states. The lowest singlet-like state was taken as GS, based on the $S^2$ value. Spin-contamination was small in all but $TS_{rot}$ structures.
4. MRSF-TDDFT was used starting from a mixed triplet ROKS reference, requesting five MRSF-TDDFT states.
5. The state-interaction state-averaged spin-restricted ensemble-referenced KS method (only REKS in the following text) was applied using perfectly spin-paired singlet, open-shell singlet and doubly excited singlet configurations. We usually first performed an RKS calculation, and the obtained orbitals were used as an initial guess for REKS. While such an approach worked well for TSs, the convergence of the REKS scheme was found to be very poor for *Z* isomers. Therefore, for the *Z* isomers, we opted for an initial guess of KS orbitals from a triplet ROKS calculation, expecting that they better approximate the averaged orbitals of the $S_0$ and $S_1$ states compared to the singlet RKS ones. Indeed, the calculations using this initial guess converged smoothly.
6. CASSCF calculations always started with the Hartree–Fock calculation using the ANO-L basis set [40] contracted to a minimal basis set (ANO-L-MB). Next, the relevant orbitals were rotated to the active space, and the CASSCF calculation was performed. The obtained orbitals were extrapolated to the ANO-L-TZVP basis set, and the final CASSCF calculation was carried out. Let us note that no core orbitals were kept frozen after the extrapolation. Molecular orbitals were visually inspected after each step. The different choices of active space are described in the Section 3. CASPT2 calculations were performed on top of the CASSCF calculations, using both state-specific (SS) and multistate-averaged (MS) approaches. In the latter case, two lowest singlet states were averaged. The zeroth-order Hamiltonian was empirically corrected using the IPEA shift of 0.25 a.u. while no imaginary shift was used.
7. The converged CASSCF wavefunction from point (6) was used in subsequent MC-PDFT calculations. In the post-CASSCF step, the tPBE functional was employed [41].
8. CCSD(T) calculations were performed in the domain-based local pair natural orbital (DLPNO) approximation [34], applying the TightPNO thresholds [42]. The same TightPNO settings were used for multireference state-specific MR-CCSD(T) [35, 36, 43], started from the CAS(2,2) reference. Explicit DLPNO values of TCutPNO, TCutPairs, TCutMKN, TCutDO thresholds were $1 \times 10^{-7}$, $1 \times 10^{-5}$, $1 \times 10^{-3}$, and $5 \times 10^{-3}$, respectively.

For the DFT-based methodologies several different functionals were used: PBE0 [44] in approaches (3–5), BHHLYP [45] in (3–5), M06-2X [37] for (1), (2), (4), CAM-B3LYP [46] and ωB97M-V [47] for (1), (2).

In all calculations, TZ quality basis sets were used. Specifically, the def2-TZVP basis set was used for all DFT, SF-TDDFT, MRSF-TDDFT, REKS, and CCSD(T) calculations. The Large Atomic Natural Orbital (ANO-L-VTZP) [40] basis set was applied in multireference CASSCF/CASPT2 and MC-PDFT calculations. Symmetry was not enforced during single point calculations.

The standard UKS/RKS calculations were performed in Gaussian 16 [48], SF-, MRSF-TDDFT and REKS were used as implemented in Gamess: version 2022 (R1) [49]. OpenMolcas [50, 51] was used for CASSCF/CASPT2 and MC-PDFT calculations. Orca version 5.0.2 was used for DLPNO-CCSD(T) and MR-CCSD(T) calculations [52, 53]. ADF version 2021 [54] was used for the natural charge analysis as part of the NBO 6.0 [55].

Thermochemical properties were evaluated at 298.15 K and 1 atm pressure using the rigid rotor and harmonic oscillator approximations.

## 2.2 | Experimental methods

The photoswitches $M_1$–$M_3$ were synthesized through azo-coupling reaction between 4-nitroaniline and 1*H*-indole (cpd $M_1$), followed by *N*-methylation of the prepared $M_1$ derivative (cpd $M_2$) or reduction of its nitro group (cpd $M_3$) (see Section S2 for details and Figures S1–S11 for NMR spectra). Fast back thermal reaction of prepared photoswitches $M_1$–$M_3$ was studied using UV–Vis spectroscopy or nanosecond laser flash photolysis technique (see Section S2, Table S1, Figures S12–S26). Corresponding photoswitching characteristics for parent $M_0$ molecule were taken from published works [21, 22, 56].

## 3 | DISCUSSION

### 3.1 | Parent $M_0$ molecule

Unsubstituted phenylazoindole $M_0$ can exist in two $Z$ forms differing by mutual orientation of the indole and phenyl moieties (see Figure 2). According to M06-2X calculations, the $Z_2$ isomer is more stable by $\Delta G = 2.5$ kcal mol$^{-1}$ in benzene, with stabilization coming from the enthalpic ($\Delta H = 1.0$ kcal mol$^{-1}$) as well as entropic contributions ($-T\Delta S = 1.5$ kcal mol$^{-1}$, Table 1). From the $Z$ minima, the $E$ isomers can be reached passing through six possible first order TSs (Figure 2).

The UKS-M06-2X calculations suggest that the rotation pathways are more accessible than inversion; however, the predicted difference between the lowest rotation ($TS_{rot2}$) and the lowest inversion ($TS_{inv1}$) barriers is small ($-1.8$ kcal mol$^{-1}$). Notably, the inversion of an indole moiety ($TS_{inv3}$, $TS_{inv4}$) is disfavored by ~4 kcal mol$^{-1}$ compared to $TS_{inv1}$, where a phenyl ring is translated to form the product. Decomposition of the $\Delta G^{\ddagger}$ values clearly indicates that the dominant factor distinguishing the thermal pathways is the activation enthalpy, which itself is governed by its electronic component (Table 1). In the non-polar benzene solvent, the IEF-PCM solvent effect ($\Delta E_{bz} - \Delta E_{gas}$) is less than 0.3 kcal mol$^{-1}$. The energetical differences sets also the trends; $R^2$ of the correlation between $\Delta E_{gas}$ and $\Delta G$ is 0.998. The influence of entropy ($-T\Delta S$ term) could be more than 1.0 kcal mol$^{-1}$ but is not systematic in determining the lowest TS.

The ordering of the TSs is different when we opt for the RKS approach. In the gas phase, the activation energy of the rotation TS becomes more than 40 kcal mol$^{-1}$ making this pathway inaccessible. For the inversion TSs and $Z$ isomers, UKS converged to the RKS solution in all cases. The RKS approach thus clearly disfavors the rotation TSs. Nevertheless, it remains an open question whether UKS correctly describes the relative heights of rotation and inversion barriers and does not bias the results in favor of the rotation mechanism.

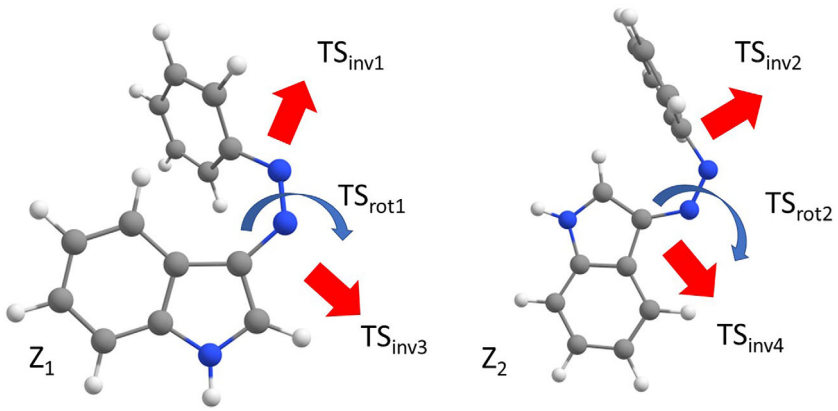


**FIGURE 2** Structures of the $Z$ isomers of $M_0$. Red arrows show which part of the azoindole molecule is moving to reach $TS_{inv}$. Blue arrows define rotational movement toward $TS_{rot}$.

**TABLE 1** Thermodynamic parameters of $M_0$ molecule calculated at the UKS-M06-2X/def2-TZVP level of theory.[a]

| Struc. | $\Delta G$ | $\Delta H$ | $\Delta E_{Bz}$[b] | $\Delta E_{gas}$ | $-T\Delta S$ |
|---|---|---|---|---|---|
| $Z_1$ | 2.5 | 1.0 | 1.0 | 1.2 | 1.5 |
| $Z_2$ | 0.0 | 0.0 | 0.0 | 0.0 | 0.0 |
| $TS_{inv1}$ | 26.5 | 26.0 | 27.2 | 27.0 | 0.5 |
| $TS_{inv2}$ | 28.8 | 28.5 | 29.9 | 29.7 | 0.2 |
| $TS_{inv3}$ | 31.3 | 30.6 | 32.0 | 32.3 | 0.7 |
| $TS_{inv4}$ | 31.8 | 30.7 | 32.0 | 32.1 | 1.2 |
| $TS_{rot1}$ | 25.1 | 23.8 | 26.2 | 26.2 (40.9) | 1.2 |
| $TS_{rot2}$ | 24.7 | 23.6 | 26.1 | 26.0 (41.1) | 1.0 |

*Note*: All values in kcal mol$^{-1}$ relative to lowest $Z$ isomer ($Z_2$).
Abbreviations: RKS, restricted Kohn–Sham; UKS, unrestricted Kohn–Sham.
[a]RKS values in parentheses.
[b]Bz denotes benzene.

Experimental half-life for $M_0$ in benzene is 54.4 ms [22], which transforms into $\Delta G^{\ddagger} = 16.0$ kcal mol$^{-1}$, using Eyring equation, temperature of 298.15 K and the transmission coefficient equal to 1. As shown in Table 1, the calculated difference between $\Delta G^{\ddagger}$ and the electronic energy $\Delta E^{\ddagger}$ is at most 2 kcal mol$^{-1}$, and thus the estimate of the experimental $\Delta E^{\ddagger}$ value in the gas phase is ≈18 kcal mol$^{-1}$, clearly smaller than the M06-2X predictions.

After establishing that the electronic activation energy in the gas phase is a good proxy for the $\Delta G^{\ddagger}$ values, we turned to more advanced methods to establish a balanced description of the transition states. Results from all methods are listed in Tables S2–S10, data important for the discussion are presented in Table 2.

A natural choice in case of the multireference character of investigated structures is the CASPT2 method. Unlike DFT, the proper settings are far from a black box approach here. We first decided to study our system with the smallest possible active space. Since only the N═N π bond is broken in $TS_{rot}$, the active space included two electrons in two orbitals: π (HOMO) and π* (LUMO) localized mainly on the N═N moiety (see Figure 3). In the second model, we also included the energetically higher combination of the azo-nitrogen's lone pairs, leading to four electrons in

**TABLE 2** Relative energies calculated using different levels of theory and estimate of the $\Delta E^{\ddagger}$ from experimental data.

| Struc | CASPT2 (2) | | CASPT2 (3, 4) | | RASPT2 (19, 22) | | DLPNO-CCSD(T) | | MC-PDFT[a] | SF-TD PBE0[b] | MRSF-TD-PBE0[b] | REKS[c] | CAM-B3LYP | ωB97M-V |
|---|---|---|---|---|---|---|---|---|---|---|---|---|---|---|
| | SS | MS | SS | MS | SS | MS | SR | MR | | | | | | |
| $Z_1$ | 0.0 | 0.2 | 0.0 | 0.0 | 0.0 | 0.0 | 1.2 | | 2.1 | 2.1 | 2.1 | 0.9 | 2.4 | 1.3 |
| $Z_2$ | 0.6 | 0.0 | 0.7 | 1.0 | 0.6 | 1.1 | 0.0 | 0.0 | 0.0 | 0.0 | 0.0 | 0.0 | 0.0 | 0.0 |
| $TS_{inv1}$ | 32.3 | 32.1 | 32.7 | 31.2 | 31.1 | 31.6 | 31.2 | 33.6 | 21.8 | 21.9 | 22.0 | 24.8 | 25.5 | 28.8 |
| $TS_{inv2}$ | 36.6 | 36.6 | 37.0 | 35.6 | 35.5 | 36.0 | 34.0 | | 23.6 | 23.8 | 23.9 | 26.8 | 27.3 | 31.3 |
| $TS_{inv3}$ | 37.7 | 37.4 | 37.9 | 37.7 | 37.6 | 39.3 | 36.2 | | 27.9 | 28.7 | 28.8 | 29.5 | 29.9 | 33.7 |
| $TS_{inv4}$ | 36.7 | 36.7 | 37.0 | 36.7 | 36.1 | 37.4 | 36.0 | | 28.0 | 29.0 | 29.1 | 29.3 | 30.3 | 33.5 |
| $TS_{rot1}$ | 31.1 | 24.4 | 32.6 | 32.4 | 37.1 | 37.1 | 42.1 | 29.4 | 29.5 | 33.1 | 32.7 | 29.8 | 18.9 | 24.5 |
| $TS_{rot2}$ | 33.5 | 25.2 | 34.6 | 33.6 | 38.5 | 38.5 | 42.1 | 29.4 | 29.3 | 32.5 | 32.0 | 29.0 | 18.2 | 24.3 |
| $\Delta E^{\ddagger}$[d] | 18.0 | | | | | | | | | | | | | |

*Note*: All values in kcal mol$^{-1}$ relative to lowest *Z* isomer.

Abbreviations: CASPT2, complete active space second-order perturbation theory; DLPNO, domain-based local pair natural orbital; MC-PDFT, multiconfiguration pair-density functional theory; MR, multireference; MRSF-TD, mixed-reference spin-flip time-dependent; RASPT2, restricted active space second-order perturbation theory; REKS, referenced Kohn–Sham; SF-TD, spin-flip time-dependent; SR, single-reference.

[a]Based on RAS(19, 22) and tPBE.

[b]Based on PBE0 functional.

[c]Based on M06-2X functional.

[d]Estimate from experiment.

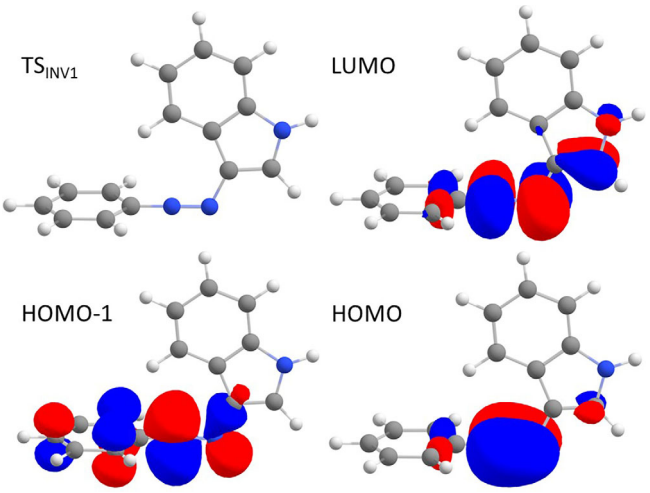


**FIGURE 3** Active space orbitals for the $TS_{inv1}$. highest occupied molecular orbital (HOMO) and least unoccupied molecular orbital (LUMO) orbitals were used for CAS(2,2) calculation, HOMO-1 was added for the CAS(3, 4). Contour value of 0.03 was used for visualization of molecular orbitals. Orbitals included in RAS(19, 22) are shown in Figure S27.

three orbitals (Figure 3). Such an active space allows a multiconfigurational relaxation of the lone pairs, which could have a stabilizing effect especially for the inversion TSs, where the nitrogen's lone pairs are clashing. The largest active space included all π and π* orbitals and nitrogen lone pairs, which corresponded to 22 electrons in 19 orbitals in total, far beyond the practical reach of CASSCF. Therefore, we applied the restricted active space (RAS) approach, allowing at most two holes in the RAS1 space and two electrons in RAS3. RAS1 comprised all 11 occupied orbitals (22 electrons), and RAS3 included 8 respective π antibonding orbitals (Figure S27). The RAS2 space remained empty.

Increasing the active space size influences the activation energy of inversion TSs only slightly, at most by 2.0 kcal mol$^{-1}$ (Table 2). The dominant configuration weight of all inversion TSs was above 0.95 confirming the single-reference character of these structures. On the other hand, the rotation TSs have clearly multireference character with the $S_0/S_1$ states being near degenerated.

The smallest CAS appears to be insufficient; the SS and MS activation energy values differ by ≈7 kcal mol$^{-1}$, which is because the ground state has different configurations in SS/MS methods. The larger CAS(3, 4) suppresses the SS/MS differences to less than 1.5 kcal mol$^{-1}$, which is however still enough to predict different orderings in the stability of TSs. In general, the CASPT2(3, 4) activation barriers are larger than those obtained by M06-2X by ≈4–5 kcal mol$^{-1}$, and the differences between the $TS_{inv1}$ and rotational TSs are smaller. The MS approach predicts that $TS_{inv1}$ is the most accessible pathway (by 1.2 kcal mol$^{-1}$), while according to the SS scheme, the $TS_{inv1}$ and $TS_{rot1}$ structures are energetically practically equivalent. The increase of the stability of $TS_{inv1}$ is even more pronounced in the RASPT2(19, 22) calculations, which for inversion TSs predict the barriers consistently with CASPT2(3, 4) but disfavor the rotation TSs. This finding can however be biased by the restricted number of allowed excitations. In any case, these results cast some doubts on the RKS/UKS ordering of the TS energies. To further investigate this issue, we employed a recently introduced MC-PDFT method which adds a DFT correction on top of the CASSCF wavefunction. We used the converged CAS and the translated PBE functional (tPBE). The results are very stable with respect to the active space choice when it comes to the ordering of TSs. Inversion is always preferred; the size of the active space affects the inversion/rotation difference, but it always remains >7 kcal mol$^{-1}$. The absolute values of the activation energies remain stable with changes <2 kcal mol$^{-1}$. The tPBE functional thus builds on the CAS reference in a more stable manner than the standard second order perturbation theory.

There is a question whether the CASPT2/RASPT2/MC-PDFT schemes sufficiently address the dynamic electron correlation effects. To pursue this issue, we performed single-reference (SR) DLPNO-CCSD(T)/def2-TZVP calculations. The CCSD(T) method is accepted as a golden standard of the computational chemistry for single reference problems. For the structures with small values of $T_1$ diagnostics and small $t_2$ amplitudes, the CCSD(T) results are very close to the RASPT2 activation energies, both in terms of the trend ($TS_{inv1}$ being smallest) and the absolute values of activation energies (Table 2). The CCSD(T) activation energies for the $TS_{rot}$ are higher than those for the inversion and thus in this aspect also follow the RASPT2 trend, but the higher values of the $T_1$ diagnostics (0.018 and 0.021 for $TS_{rot1}$ and $TS_{rot2}$, respectively) and large $t_2$ amplitudes lower the credibility of CC results for these structures (for the CC diagnostics of all structures see Table S11). Multireference (MR) CC approaches are the obvious candidates to resolve this issue. We applied Mukherjee MR-CC, DLPNO-Mk-MR-CCSD(T), with a reference space of two electrons and two orbitals (2). The $TS_{rot}$ structures are largely stabilized with the activation energy of 29.4 kcal mol$^{-1}$ (Table 2). The switching between $TS_{inv}$ and $TS_{rot}$ appears after addition of the perturbative triples (*T*) correction. The Mk-MR-CCSD(T) results follow the same trend as CASPT2(2), which is apparently related to the application of the same active space. Together with SR-CCSD(T) following the RKS trends, we can conclude the dynamical electron correlation plays a less important role compared to the static correlation in this particular application.

The MC-PDFT method connecting the multireference character with DFT was shown to be a suitable approach for the consistent description of both types of TSs. Nevertheless, its accuracy depends on the CAS size and for large active spaces becomes computationally demanding. Therefore, we assessed three other DFT methods developed to increase the applicability of standard DFT to quasi-degenerate systems, namely SF-TDDFT, MRSF-TDDFT, and REKS, as faster and more black box approaches possibly able to scan large swaths of azobenzene chemical space. The choice of a DFT functional for all three methods is an important factor. We picked PBE0 as a representative of global hybrids, also for its good performance in previous benchmarks by Adrion et al. [23] Spin-contamination is a frequent problem for spin-flip methods, and the usual remedy is a higher percentage of the exact exchange in the applied functional. Therefore, we also used BHHLYP containing 50% of the HF exchange. Finally, the M06-2X functional used in our initial analysis was also tested (see Section S3 for all results). All three methods independently on the choice of the functional predict $TS_{inv1}$ as the most accessible TS. The global hybrid PBE0 functional with a small fraction of the HF exchange always yields a large difference between rotation and inversion: 10 kcal mol$^{-1}$ when adopted in SF/MRSF and 4 kcal mol$^{-1}$ when employed inside the REKS approach. Higher amounts of the HF exchange in BHHLYP and M06-2X tend to decrease the inversion/rotation gap in SF-TDDFT and MRSF-TDDFT, while REKS does not show this behavior. On the other hand, the absolute activation energies predicted by BHHLYP and M06-2X (as SF, MRSF, and REKS) are closer to those obtained by the CCSD(T) and RASPT2 references. The spin contamination is large for the $TS_{rot}$ structures when using SF-TDDFT methods, but it is certainly smaller compared to U-M06-2X calculation, where $S^2 = 1.04$. The MRSF method significantly improves on this issue, obtaining contamination-free singlet $TS_{rot}$ states. Unfortunately, the range-separated functionals cannot be currently employed within MRSF/REKS schemes. Applied within standard UKS, both CAM-B3LYP and ωB97M-V follow the trend attained by M06-2X favoring the rotation mechanism but tend to decrease the barriers, thus bringing them closer to the experimental reference, in paricular in the case of CAM-B3LYP. Let us note that the ωB97M-V functional was recently found successful in predicting reaction barriers for an extensive benchmark set of chemical reactions, although without double bond torsion reactions [57].

Estimate of the experimental $\Delta E^{\ddagger}$ in the gas phase is ≈18 kcal mol$^{-1}$. The CAM-B3LYP method predicts value of 18.2 kcal mol$^{-1}$ for $TS_{rot2}$. All other applied methods show higher $\Delta E^{\ddagger}$, MC-PDFT is close to $\Delta E^{\ddagger} = 21.8$ kcal mol$^{-1}$, followed by PBE0 versions of SF, MRSF and REKS methods.

Figure 4 visually summarizes the results discussed so far. All methods follow the same trend within the inversion group, clearly identifying $TS_{inv1}$ as the lowest reaction barrier. Similarly, all methods confirm the near equivalence of the two rotational TSs. However, the identification of the rotation/inversion pathway in the isomerization of $M_0$ strongly depends on the applied methods. For DFT based methods, the choice of functional and spin-restriction formalism are very influential factors. On the other hand, for CAS methods, the choice of the active space can significantly affect the available reaction pathways. Both restricted singe-reference methods, RKS and CCSD(T), significantly disfavor the rotational mechanism due to the failed MR description. Inversely, UKS overcompensates on account of high spin contamination. The MC-PDFT method seems to be robust against incomplete choice of the active space, predicting consistently the same mechanism and comparable activation energies across different active spaces (Tables 2 and S10). The MRSF and REKS methods represent spin-contamination-free DFT approaches, with the PBE0 functional providing results closely following the RASPT2 trends. All methods overshoot the experiment by about 5–15 kcal mol$^{-1}$, with DFT data being closer to experiment, while *ab initio* methods show higher precision and more tightly clustered trends (for the inversion barriers).

## 3.2 | Effects of solvent and substitution

In the previous section we detailed calculations in the gas phase. Although such a comparison is methodologically interesting, azoindoles are medium sized molecules intended for use in solvent environments. We performed experiments in two solvents, in nonpolar benzene and in polar dimethyl sulfoxide (DMSO). Both are aprotic, eliminating the possible proton transfer and intermolecular azo-hydrazone tautomerization reactions (Figure 5). This mechanism can also be excluded based on the comparison between $M_1$ and its *N*-methylated derivative $M_2$. The methyl

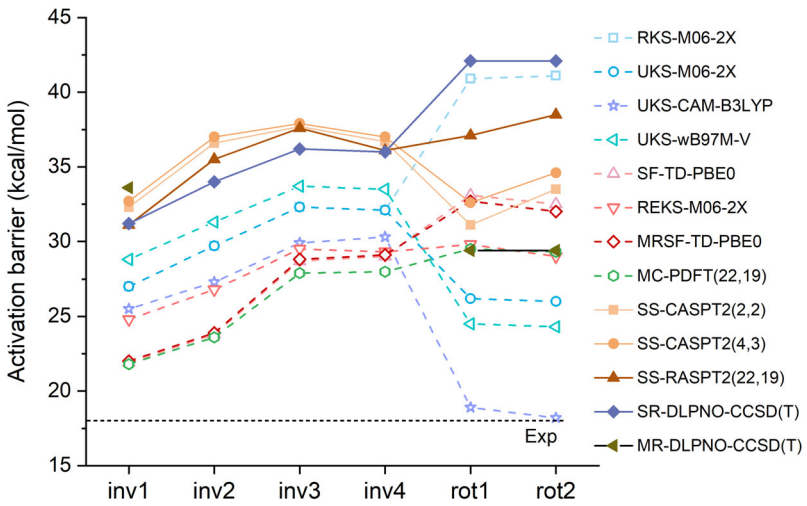


**FIGURE 4** Comparison of activation barriers obtained with different density functional theory (DFT) (dashed) and *ab initio* (full) methods. Lines serve as a guide for the eye. Experimental gas phase value was estimated from the barrier measured in benzene and computed thermal ($\Delta G^{\ddagger} - \Delta E^{\ddagger}$) and solvent contributions (see text).

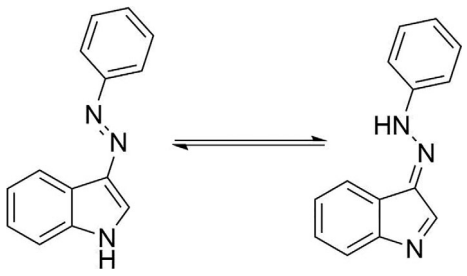


**FIGURE 5** Possible tautomerization reaction of studied phenylazoindoles.

**TABLE 3** Experimental and calculated $\Delta G^{\ddagger}$ (kcal mol$^{-1}$) values for thermal *Z*-to-*E* reaction.

| Solvt./$\Delta G^{\ddagger}$ | $M_0$ | $M_1$ | $M_2$ | $M_3$ |
|---|---|---|---|---|
| *Experiment* | | | | |
| Bz | 16.0 | 18.7 | 20.0 | 15.6 |
| DMSO | 18.6 | 14.7 | 13.7 | 14.9 |
| $\Delta G^{\ddagger}$(M06-2X) | | | | |
| Bz | 24.7 (rot) | 19.1 (inv) | 18.9 (inv) | 21.7 (rot) |
| DMSO | 24.4 (rot) | 18.1 (inv) | 18.1 (inv) | 21.1 (rot) |
| $\Delta G^{\ddagger}$(CAM-B3LYP) | | | | |
| Bz | 16.9 (rot) | 16.6 (rot) | 15.9 (rot) | 14.1 (rot) |
| DMSO | 16.9 (rot) | 16.7 (inv) | 16.7 (inv) | 14.0 (rot) |
| $\Delta G^{\ddagger}$(ωB97M-V) | | | | |
| Bz | 23.0 (rot) | 22.0 (inv) | 22.0 (inv) | 20.1 (rot) |
| DMSO | 22.7 (rot) | 21.3 (inv) | 21.5 (inv) | 19.5 (rot) |
| $\Delta G^{\ddagger}$(MRSF-TD-PBE0) | | | | |
| Bz | 22.1 (inv) | 12.8 (inv) | 12.6 (inv) | 25.7 (inv) |
| DMSO | 22.3 (inv) | 12.1 (inv) | 12.5 (inv) | 24.6 (rot) |
| $\Delta G^{\ddagger}$(MRSF-TD-BHHLYP) | | | | |
| Bz | 26.4 (rot) | 20.5 (inv) | 20.3 (inv) | 22.7 (rot) |
| DMSO | 25.4 (rot) | 20.1 (inv) | 20.7 (inv) | 21.1 (rot) |
| $\Delta G^{\ddagger}$(CCSD(T)) | | | | |
| Bz | 30.8 (inv) | 24.8 (inv) | 25.0 (inv) | 33.9 (inv) |
| DMSO | 30.7 (inv) | 24.2 (inv) | 24.5 (inv) | 34.7 (inv) |

*Note*: In all cases electronic part of the $\Delta G^{\ddagger}$ comes from respective method and the rest comes from the M06-2X calculation. In parenthesis is predicted isomerization mechanism.

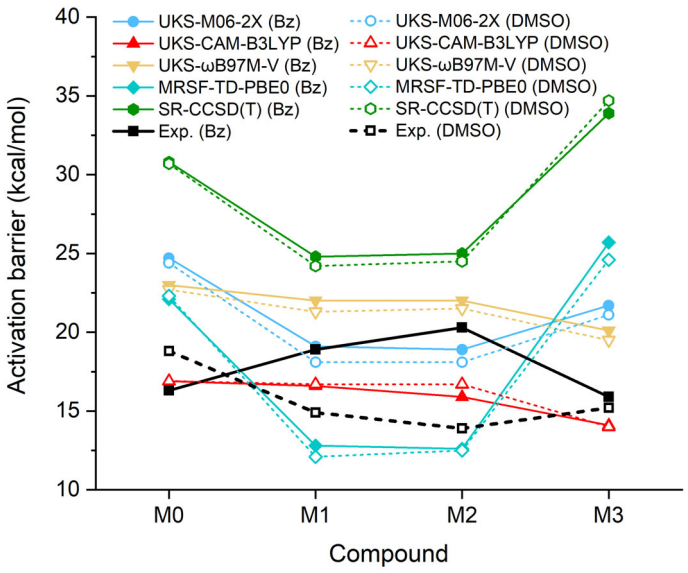


**FIGURE 6** Experimental and calculated $\Delta G^{\ddagger}$ (kcal mol$^{-1}$) values for thermal *Z*-to-*E* reaction. Note that the M06-2X vibrational contributions are added to the electronic energies calculated at different levels of theory to obtain the $\Delta G^{\ddagger}$ values.

substitution effectively blocks the tautomerization, yet the reaction barriers are within 1 kcal mol$^{-1}$ compared to the structurally similar $M_1$ for both solvents (Table 3).

Our analysis of the trends in the studied group starts with a simple question—Can we predict reaction mechanism based on the changes in reaction barriers between benzene and DMSO? To answer this, we applied several successful methods tested in previous chapter: M06-2X,

CAM-B3LYP, ωB97M-V, MRSF-PBE0, and SR-CCSD(T) (in case of inversion only) employing the continuum solvent model for benzene and DMSO. The experimental and theoretical results are summarized in Table 3, and the overall trends can be seen in Figure 6. As was shown in the previous section, vibrational contributions to the $\Delta G^{\ddagger}$ do not change the overall picture based on the electronic energies $\Delta E^{\ddagger}$ (see also Section S3, Figure S27). We thus include the vibrational and thermal contributions calculated at the M06-2X level in all cases for better comparison with experiment and base our discussion of reaction mechanisms on electronic activation energies only.

We experimentally observed that the substitution and solvent tune the thermal barriers to a large extent (Figure 6). In benzene, the *push-pull* systems $M_1$ and $M_2$ have the largest barriers. In DMSO, the situation reverses with $M_1$ and $M_2$ becoming the fastest switches in the studied group. Computationally, MRSF-PBE0, CCSD(T), and M06-2X predict the DMSO-like trend already in benzene. For CCSD(T), this can be understood as the RHF reference disfavors rotation, which is the most probable mechanism for $M_0$ and $M_3$ (Table 3) as we also discuss below in more details. Inversion is thus higher in energy, creating the characteristic boat-like trend in Figure 6 already for benzene. All used methods, except for CAM-B3LYP, support the inversion ($TS_{inv}$) as the most accessible pathway for $M_1$ and $M_2$ molecules (Table 3) and show decrease of activation energy with the increasing solvent polarity, albeit this effect is smaller compared to experiment. The CAM-B3LYP functional predicts rotation as the most accessible pathway in benzene and inversion in DMSO. However, it should be noted that the differences between $TS_{inv}$ and $TS_{rot}$ were found to be very small (<0.6 kcal mol$^{-1}$). The two range-separated functionals, CAM-B3LYP and ωB97M-V, show the most promising results with $M_0$–$M_2$ having almost the same barriers while $M_3$ has the smallest one in benzene. Molecule $M_0$ was of particular experimental interest due to the unexpected increase in the half-life of the *Z* isomer in DMSO. MRSF-PBE0 with the C-PCM solvent model can follow this trend, while CAM-B3LYP shows no change. Unlike for other molecules, for $M_0$ we found the change of non-electronic contributions of $\Delta G^{\ddagger}$ non-negligible and negative, thus canceling the small positive electronic contributions (Section S3, Figure S27).

Since the solvent effects are visibly underestimated compared to experiment (Figure 6), in the following, we analyze them separately to aid our discussion. Figure 7 shows the pure solvent effects as a net change in electronic activation energy $E^{\ddagger}$ between the nonpolar benzene (see Table S12) and polar DMSO calculated for both rotation and inversion mechanisms in comparison with experimental observation. For inversion, we see a uniform picture across all selected methods. The barrier should increase when going from benzene to DMSO for $M_0$ and $M_3$ molecules, but a decrease is predicted for $M_1$ and $M_2$. The predicted behavior of $M_0$–$M_2$ is qualitatively consistent with experiment, corroborating the inversion mechanism in these species. For rotation, all calculations predict the $M_3$ barrier to decrease in polar DMSO. This is in turn consistent with experiment, suggesting the rotation mechanism for $M_3$. For $M_0$–$M_2$, there is no clear agreement between the changes to $TS_{rot}$ barriers predicted by different methods. Furthermore, the situation is more complicated in case of $M_0$ due to a larger vibrational contribution to $\Delta G^{\ddagger}$ with change of solvent, and we thus cannot decide on the mechanism based on this observation solely. Another general observation visible from Figure 7 is that the solvent shifts based on the polarizable continuum solvation (PCM) model employed here are about 4–5 times smaller compared to their experimental counterparts. Adding upscaled solvent effects to the gas phase $\Delta E^{\ddagger}$ would improve experiment-theory agreement especially when using the RSH CAM-B3LYP functional.

The solvent effects on the reaction barriers are related to the difference in polarity of the *Z* isomer and the TS. The azoindole molecule can be divided into three regions: the indole moiety, the azo bridge, and the phenyl group. Figure 8 shows summed natural charges for each part of the molecule. Clearly, indole is an electron donating moiety and the azo bridge is negatively charged. When substituting phenyl with —$NO_2$, the corresponding *Z* isomers ($M_1$, $M_2$) become more polarized, with observable electron pull from the indole group. The expected reversed effect is,

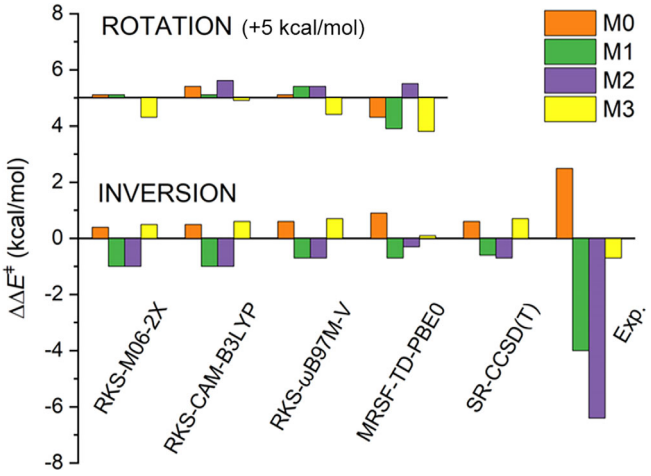


**FIGURE 7** Comparison of activation barriers changes, $\Delta\Delta E^{\ddagger} = \Delta E^{\ddagger}(\text{DMSO}) - \Delta E^{\ddagger}(\text{benzene})$, for experiment and selected methods. All values are in kcal mol$^{-1}$. Baseline for solvent effects on rotational barriers was shifted by 5 kcal mol$^{-1}$ for the convenience of direct comparison with inversion.

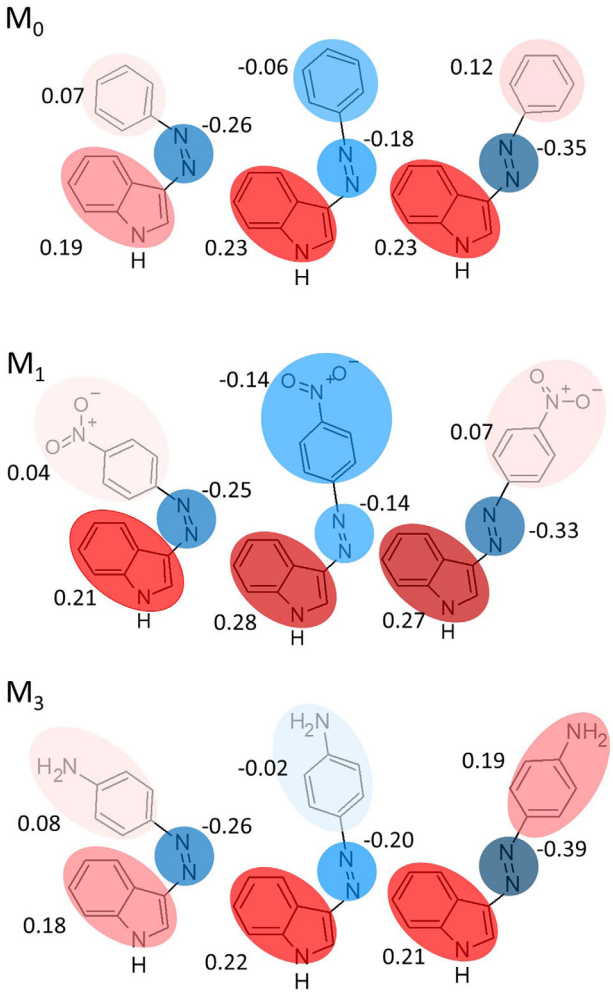


**FIGURE 8** Natural charges summed to three distinct regions of the $M_0$ (top) $M_1$ (middle) and $M_3$ (bottom) for the *Z* isomer, $TS_{rot}$ and $TS_{inv}$. Calculated using the M06-2X functional in the gas phase. Charges of $M_2$ are near identical to those of $M_1$, hence it was omitted from the figure.

however, not seen in the case of the amino group in $M_3$. The azo group remains constantly charged in all *Z* isomers. General observations can also be made about the two competing mechanisms. All $TS_{rot}$ structures feature a more negatively charged azo bridge and a more positively charged phenyl moiety compared to the *Z* isomer, while the opposite is true for all $TS_{inv}$'s. Combination of these substitution (vertical) and mechanism (horizontal) trends shown in Figure 7 leads to several noteworthy conclusions:

1. Inversion TS is more polarized in the *push-pull* systems $M_1$ and $M_2$ since the inverting nitrophenyl moiety becomes strongly negatively charged and more charge is also pulled from the indole group. In contrast, $TS_{inv}$ for $M_0$ and $M_3$ lacks such a strong redistribution of charge since inverting phenyl (aminophenyl) groups are electron donating. Observed changes in charge distribution corroborate the changes in reaction barriers where the inversion barriers of the *push-pull* molecules decrease in more polar solvents but increase for $M_0$ and $M_3$ (Figure 6).
2. The increased negative charge of the azo moiety in $TS_{rot}$ compared to the *Z* isomer for $M_1$ and $M_2$ comes at the cost of electron transfer from indole and electron accepting nitrophenyl electron distribution remains intact. In $TS_{rot}$ of $M_3$, the charging of the central azo group comes from both indole and aminophenyl groups, leading to a more polar TS compared to *Z*, again corroborating calculated shifts in the rotation barrier. In $M_0$, $TS_{rot}$ is more charged in all defined areas, yet this increase is rather small compared to, for example, $TS_{rot}$ of $M_3$.

## 4 | CONCLUSIONS

Heteroarene-based azobenzene photoswitches offer many promising properties and are a hot area of research. In our contribution we prepared, experimentally characterized and computationally studied the switching of a small group of phenylazoindole molecules. Several different levels of

theory were used to establish the mechanism and activation barrier heights of thermal back-reaction including solvent effects. Despite the extensive methodological study of $M_0$ in the gas phase, a single definite recommendation for the best method cannot be offered. In systems, such as the presently investigated phenylazoindoles, where MR description of the species is necessary, even the approaches generally viewed as reliable did not provide consistent ordering of TSs. The size of the systems did not allow us to reach the convergence of MR approaches with respect to all necessary parameters (e.g., the size of the active space in CASPT2/MR-CC and the number of allowed excitations in RASPT2/MC-PDFT). The derived push-pull systems ($M_1$, $M_2$) were found to be less sensitive to the applied approach, which can be related to the stabilization of a particular TS in solvent. For the $M_1$ and $M_2$ molecules, we conclude, based on both $\Delta G^{\ddagger}$ and solvent effects, that inversion is the preferable mechanism. For the $M_3$, rotation is preferred. Mechanism of the $M_0$ molecule remains undecided based on our calculations. Our work comes as a warning of many potential threats hidden behind the scene when comparing the seemingly uniform group of azobenzenes. Establishing mechanism requires multireference calculations with inclusion of dynamic correlation, yet the balanced description of both inversion and torsion becomes even more important in the solvent, where addition of the solvent can eventually change the mechanism. We have found that continuum solvation models underestimate the influence of solvents resulting in the ordering of molecules which contradicts experimental trends. For future studies it is advised to consider experimental and theoretical data in several solvents rather than concentrating efforts on reaching experiment-theory agreement in one solvent. For the present set, range-separated functionals offer the most balanced description of substitutional effects, which would after the upscaling of the solvent effects reflect the experimental trends in thermal barriers.

## FUNDING INFORMATION

Authors acknowledge the support of the Slovak Research and Development Agency and the Scientific Grant Agency, APVV-20-0098 and VEGA 1/0562/20, respectively.

## DATA AVAILABILITY STATEMENT

The data that support the findings of this study are available from the corresponding author upon reasonable request.

## RESEARCH RESOURCES

This research used resources of the High-Performance Computing Center of the Matej Bel University in Banská Bystrica.

## ORCID

*Miroslav Medved'* https://orcid.org/0000-0001-8599-1031
*Lukáš Félix Pašteka* https://orcid.org/0000-0002-0617-0524
*Marek Cigáň* https://orcid.org/0000-0001-7734-626X
*Šimon Budzák* https://orcid.org/0000-0003-4811-8342

## REFERENCES

[1] F. A. Jerca, V. V. Jerca, R. Hoogenboom, *Nat. Rev. Chem.* **2021**, *6*, 51.
[2] J. Calbo, C. E. Weston, A. J. P. White, H. S. Rzepa, J. Contreras-García, M. J. Fuchter, *J. Am. Chem. Soc.* **2017**, *139*, 1261.
[3] S. Axelrod, E. Shakhnovich, R. Gomez-Bombarelli, *Nat. Commun.* **2022**, *13*, 3440.
[4] A. Kerckhoffs, K. E. Christensen, M. J. Langton, *Chem. Sci.* **2022**, *13*, 11551.
[5] J. Garcia-Amorós, M. Díaz-Lobo, S. Nonell, D. Velasco, *Angew. Chem. Int. Ed.* **2012**, *51*, 12820.
[6] I. Tochitsky, M. A. Kienzler, E. Isacoff, R. H. Kramer, *Chem. Rev.* **2018**, *118*, 10748.
[7] D. Bléger, J. Schwarz, A. M. Brouwer, S. Hecht, *J. Am. Chem. Soc.* **2012**, *134*, 20597.
[8] L. N. Lameijer, S. Budzak, N. A. Simeth, M. J. Hansen, B. L. Feringa, D. Jacquemin, W. Szymanski, *Angew. Chem. Int. Ed.* **2020**, *59*, 21663.
[9] M. Dong, A. Babalhavaeji, C. V. Collins, K. Jarrah, O. Sadovski, Q. Dai, G. A. Woolley, *J. Am. Chem. Soc.* **2017**, *139*, 13483.
[10] A. A. Beharry, G. A. Woolley, *Chem. Soc. Rev.* **2011**, *40*, 4422.
[11] C. Fedele, T. P. Ruoko, K. Kuntze, M. Virkki, A. Priimagi, *Photochem. Photobiol. Sci.* **2022**, *1*, 1.
[12] H. B. Cheng, S. Zhang, J. Qi, X. J. Liang, J. Yoon, *Adv. Mater.* **2021**, *33*, 2007290.
[13] H. M. D. Bandara, S. C. Burdette, *Chem. Soc. Rev.* **2012**, *41*, 1809.
[14] V. Marturano, V. Ambrogi, N. A. G. Bandeira, B. Tylkowski, M. Giamberini, P. Cerruti, *Phys. Sci. Rev.* **2017**, *2*, 20170138.
[15] A. Cembran, F. Bernardi, M. Garavelli, L. Gagliardi, G. Orlandi, *J. Am. Chem. Soc.* **2004**, *126*, 3234.
[16] J. Dokić, M. Gothe, J. Wirth, M. V. Peters, J. Schwarz, S. Hecht, P. Saalfrank, *J. Phys. Chem. A* **2009**, *113*, 6763.
[17] C. E. Weston, R. D. Richardson, P. R. Haycock, A. J. P. White, M. J. Fuchter, *J. Am. Chem. Soc.* **2014**, *136*, 11878.
[18] J. Simke, T. Bösking, B. J. Ravoo, *Org. Lett.* **2021**, *23*, 7635.
[19] J. Calbo, A. R. Thawani, R. S. L. Gibson, A. J. P. White, M. J. Fuchter, *Beilstein J. Org. Chem.* **2019**, *15266*(15), 2753.
[20] Y. He, Z. Shangguan, Z.-Y. Zhang, M. Xie, C. Yu, T. Li, *Angew. Chem.* **2021**, *133*, 16675.
[21] S. Crespi, N. A. Simeth, A. Bellisario, M. Fagnoni, B. König, *J. Phys. Chem. A* **2019**, *123*, 1814.
[22] N. A. Simeth, S. Crespi, M. Fagnoni, B. König, *J. Am. Chem. Soc.* **2018**, *140*, 2940.
[23] D. M. Adrion, D. S. Kaliakin, P. Neal, S. A. Lopez, *J. Phys. Chem. A* **2021**, *125*, 6474.
[24] M. Poutanen, Z. Ahmed, L. Rautkari, O. Ikkala, A. Priimagi, *ACS Macro Lett.* **2018**, *7*, 381.

[25] A. Muždalo, P. Saalfrank, J. Vreede, M. Santer, *J. Chem. Theory Comput.* **2018**, *14*, 2042.
[26] G. Li Manni, R. K. Carlson, S. Luo, D. Ma, J. Olsen, D. G. Truhlar, L. Gagliardi, *J. Chem. Theory Comput.* **2014**, *10*, 3669.
[27] R. K. Carlson, G. Li Manni, A. L. Sonnenberger, D. G. Truhlar, L. Gagliardi, *J. Chem. Theory Comput.* **2015**, *11*, 82.
[28] M. Filatov, *Wiley Interdiscip. Rev. Comput. Mol. Sci.* **2015**, *5*, 146.
[29] Y. Shao, M. Head-Gordon, A. I. Krylov, *J. Chem. Phys.* **2003**, *118*, 4807.
[30] D. Casanova, A. I. Krylov, *Phys. Chem. Chem. Phys.* **2020**, *22*, 4326.
[31] Y. Horbatenko, S. Sadiq, S. Lee, M. Filatov, C. H. Choi, *J. Chem. Theory Comput.* **2021**, *17*, 848.
[32] K. Andersson, P. Å. Malmqvist, B. O. Roos, A. J. Sadlej, K. Wolinski, *J. Phys. Chem.* **1990**, *94*, 5483.
[33] K. Andersson, P. Å. Malmqvist, B. O. Roos, *J. Chem. Phys.* **1992**, *96*, 1218.
[34] C. Riplinger, P. Pinski, U. Becker, E. F. Valeev, F. Neese, *J. Chem. Phys.* **2016**, *144*, 024109.
[35] J. Brabec, J. Lang, M. Saitow, J. Pittner, F. Neese, O. Demel, *J. Chem. Theory Comput.* **2018**, *14*, 1370.
[36] O. Demel, J. Pittner, F. Neese, *J. Chem. Theory Comput.* **2015**, *11*, 3104.
[37] Y. Zhao, D. G. Truhlar, Y. Zhao, D. G. Truhlar, *Theor. Chem. Acc.* **2007**, *120*, 215.
[38] F. Weigend, R. Ahlrichs, *Phys. Chem. Chem. Phys.* **2005**, *7*, 3297.
[39] E. Cancès, B. Mennucci, J. Tomasi, *J. Chem. Phys.* **1997**, *107*, 3032.
[40] P. O. Widmark, P. Å. Malmqvist, B. O. Roos, *Theor. Chim. Acta* **1990**, *77*, 291.
[41] R. K. Carlson, D. G. Truhlar, L. Gagliardi, *J. Chem. Theory Comput.* **2015**, *11*, 4077.
[42] D. G. Liakos, M. Sparta, M. K. Kesharwani, J. M. L. Martin, F. Neese, *J. Chem. Theory Comput.* **2015**, *11*, 1525.
[43] K. Bhaskaran-Nair, O. Demel, J. Šmydke, J. Pittner, *J. Chem. Phys.* **2011**, *134*, 154106.
[44] C. Adamo, V. Barone, *J. Chem. Phys.* **1999**, *110*, 6158.
[45] A. D. Becke, *J. Chem. Phys.* **1993**, *98*, 1372.
[46] T. Yanai, D. P. Tew, N. C. Handy, *Chem. Phys. Lett.* **2004**, *393*, 51.
[47] N. Mardirossian, M. Head-Gordon, *J. Chem. Phys.* **2016**, *144*, 214110.
[48] M. J. Frisch, G. W. Trucks, H. B. Schlegel, G. E. Scuseria, M. A. Robb, J. R. Cheeseman, G. Scalmani, V. Barone, G. A. Petersson, H. Nakatsuji, X. Li, M. Caricato, A. V. Marenich, J. Bloino, B. G. Janesko, R. Gomperts, B. Mennucci, H. P. Hratchian, J. V. Ortiz, A. F. Izmaylov, J. L. Sonnenberg, F. D. Williams, F. Lipparini, F. Egidi, J. Goings, B. Peng, A. Petrone, T. Henderson, D. Ranasinghe, V. G. Zakrzewski, J. Gao, N. Rega, G. Zheng, W. Liang, M. Hada, M. Ehara, K. Toyota, R. Fukuda, J. Hasegawa, M. Ishida, T. Nakajima, Y. Honda, O. Kitao, H. Nakai, T. Vreven, K. Throssell, J. A. Montgomery Jr., J. E. Peralta, F. Ogliaro, M. J. Bearpark, J. J. Heyd, E. N. Brothers, K. N. Kudin, V. N. Staroverov, T. A. Keith, R. Kobayashi, J. Normand, K. Raghavachari, A. P. Rendell, J. C. Burant, S. S. Iyengar, J. Tomasi, M. Cossi, J. M. Millam, M. Klene, C. Adamo, R. Cammi, J. W. Ochterski, R. L. Martin, K. Morokuma, O. Farkas, J. B. Foresman, D. J. Fox, *Gaussian 16, Revision A.01*, Gaussian, Inc., Wallingford, CT **2016**.
[49] G. M. J. Barca, C. Bertoni, L. Carrington, D. Datta, N. De Silva, J. E. Deustua, D. G. Fedorov, J. R. Gour, A. O. Gunina, E. Guidez, T. Harville, S. Irle, J. Ivanic, K. Kowalski, S. S. Leang, H. Li, W. Li, J. J. Lutz, I. Magoulas, J. Mato, V. Mironov, H. Nakata, B. Q. Pham, P. Piecuch, D. Poole, S. R. Pruitt, A. P. Rendell, L. B. Roskop, K. Ruedenberg, T. Sattasathuchana, M. W. Schmidt, J. Shen, L. Slipchenko, M. Sosonkina, V. Sundriyal, A. Tiwari, J. L. Galvez Vallejo, B. Westheimer, M. Włoch, P. Xu, F. Zahariev, M. S. Gordon, *J. Chem. Phys.* **2020**, *152*, 154102.
[50] F. Aquilante, J. Autschbach, A. Baiardi, S. Battaglia, V. A. Borin, L. F. Chibotaru, I. Conti, L. De Vico, M. Delcey, I. F. Galván, N. Ferré, L. Freitag, M. Garavelli, X. Gong, S. Knecht, E. D. Larsson, R. Lindh, M. Lundberg, P. Å. Malmqvist, A. Nenov, J. Norell, M. Odelius, M. Olivucci, T. B. Pedersen, L. Pedraza-González, Q. M. Phung, K. Pierloot, M. Reiher, I. Schapiro, J. Segarra-Martí, F. Segatta, L. Seijo, S. Sen, D. C. Sergentu, C. J. Stein, L. Ungur, M. Vacher, A. Valentini, V. Veryazov, *J. Chem. Phys.* **2020**, *152*, 214117.
[51] I. Fdez, M. Galván, A. Vacher, C. Alavi, F. Angeli, J. Aquilante, J. J. Autschbach, S. I. Bao, N. A. Bokarev, R. K. Bogdanov, L. F. Carlson, J. Chibotaru, N. Creutzberg, M. G. Dattani, S. S. Delcey, A. Dong, L. Dreuw, L. M. Freitag, L. Frutos, F. Gagliardi, A. Gendron, L. Giussani, G. González, M. Grell, C. E. Guo, M. Hoyer, S. Johansson, S. Keller, G. Knecht, E. Kovačević, G. L. Källman, M. Manni, Y. Lundberg, S. Ma, J. P. Mai, P. Å. Malhado, P. Malmqvist, S. A. Marquetand, J. Mewes, M. Norell, M. Olivucci, Q. M. Oppel, K. Phung, F. Pierloot, M. Plasser, A. M. Reiher, I. Sand, P. Schapiro, C. J. Sharma, L. K. Stein, D. G. Sørensen, M. Truhlar, L. Ugandi, A. Ungur, S. Valentini, V. Vancoillie, O. Veryazov, T. A. Weser, P. O. Wesołowski, S. Widmark, A. Wouters, J. P. Z. Zech, R. Lindh, *J. Chem. Theory Comput.* **2019**, *15*, 5925.
[52] F. Neese, F. Wennmohs, U. Becker, C. Riplinger, *J. Chem. Phys.* **2020**, *152*, 224108.
[53] F. Neese, *Wiley Interdiscip. Rev. Comput. Mol. Sci.* **2022**, *12*, e1606.
[54] G. te Velde, F. M. Bickelhaupt, E. J. Baerends, C. Fonseca Guerra, S. J. A. van Gisbergen, J. G. Snijders, T. Ziegler, *J. Comput. Chem.* **2001**, *22*, 931.
[55] E. D. Glendening, C. R. Landis, F. Weinhold, *J. Comput. Chem.* **2013**, *34*, 1429.
[56] N. A. Simeth, A. Bellisario, S. Crespi, M. Fagnoni, B. König, *J. Org. Chem.* **2019**, *84*, 6565.
[57] G. Santra, R. Calinsky, J. M. L. Martin, *J. Phys. Chem. A* **2022**, *126*, 5492.

## SUPPORTING INFORMATION

Additional supporting information can be found online in the Supporting Information section at the end of this article.

**How to cite this article:** L. Hegedüsová, R. Kutel', M. Medved', L. F. Pašteka, M. Cigáň, Š. Budzák, *Int. J. Quantum Chem.* **2023**, *123*(24), e27120. https://doi.org/10.1002/qua.27120